Electronic Supplementary Material (ESI) for Journal of Materials Chemistry A.

This journal is © The Royal Society of Chemistry 2022

Electronic Supplementary Information

Constructing asymmetrical dual catalytic sites in manganese oxides enables fast and stable lithium-oxygen catalysis

Bo Liu, Xinmiao Liu, Cong Wei, Ya Zhou, Zixuan Zhu, Xin Lei, Yanyan Fang, Yida Zhang, Jun Liu*, Yitai Qian and Gongming Wang*

Experimental Section

Surface models: Based on XRD and HR-TEM characterization results, the catalyst surface models were based on the (200) oriented surface of the Ru SAs@MnO_2 crystal structure. Furthermore, combined with fine structure characterization (HAADF-STEM and XANES), the tendency of Ru SAs to replace Mn on the MnO_2 surface was considered. We model the Ru SAs@MnO_2 catalyst by replacing surface Mn atom with a Ru atom on the MnO_2(100) surface, denoted as Ru SAs@MnO_2(100). A four-layer, $p(1 \times 4)$ Ru SAs@MnO_2(100), where each layer includes 8 Mn atoms and 16 O atoms (see Fig. S15†). In addition, MnO_2(100) surfaces of the same size were constructed for comparison. Furthermore, the repeated slabs were separated from their neighboring images by a 15 Å width vacuum in the direction perpendicular to the surface. In all calculations, the bottom two layers (including 32 oxygen atoms and 16 manganese atoms) were fixed to their buck positions and the other layers with the adsorbed species were allowed to relax.

Supplementary Figures

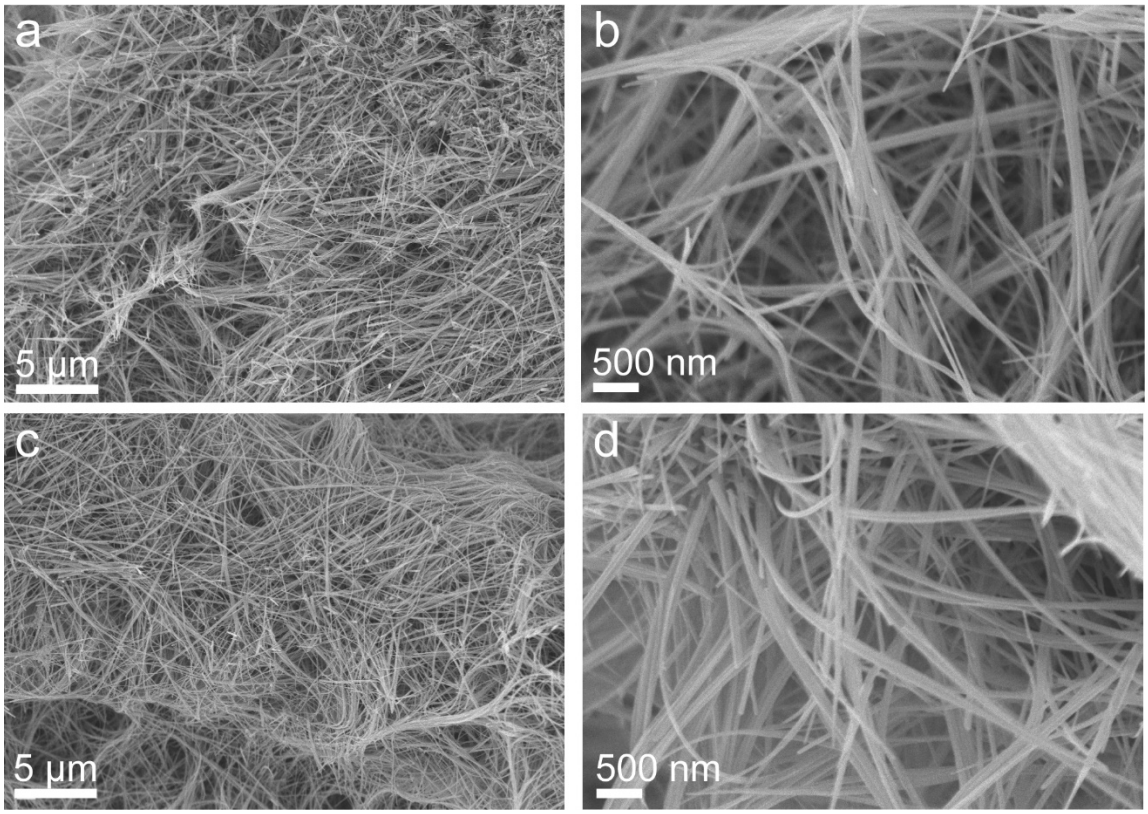

Fig. S1 SEM images of (a, b) MnO_2 nanowires, and (c, d) Ru SAs@MnO_2, respectively.

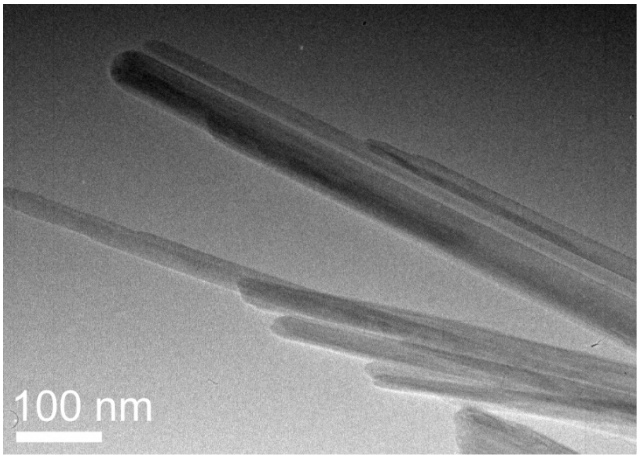

Fig. S2 The TEM image of Ru SAs@MnO_2.

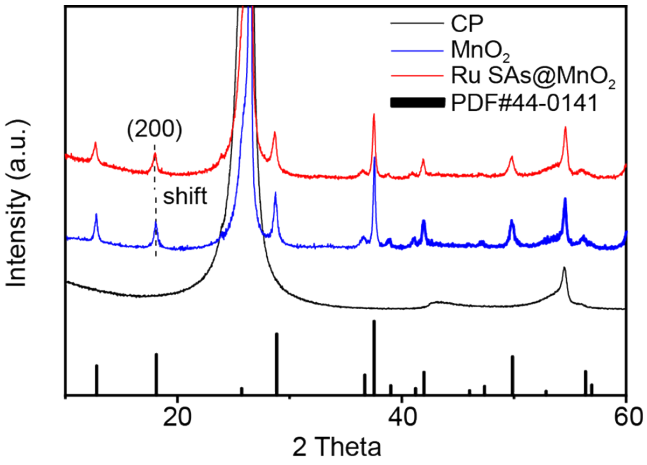

Fig. S3 XRD patterns of Ru SAs@MnO_2, MnO_2, and CP samples.

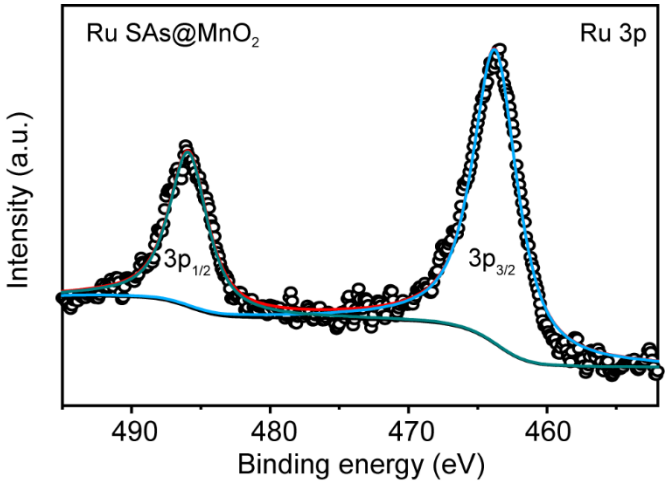

Fig. S4 The high-resolution XPS spectrum of Ru 3p in Ru SAs@MnO_2 sample.

For the Ru SAs@MnO_2 sample, the peaks of Ru $3p_{3/2}$ and Ru $3p_{1/2}$ located at 463.7 and 485.9 eV, respectively, revealing the oxidation state of Ru species.[1, 2]

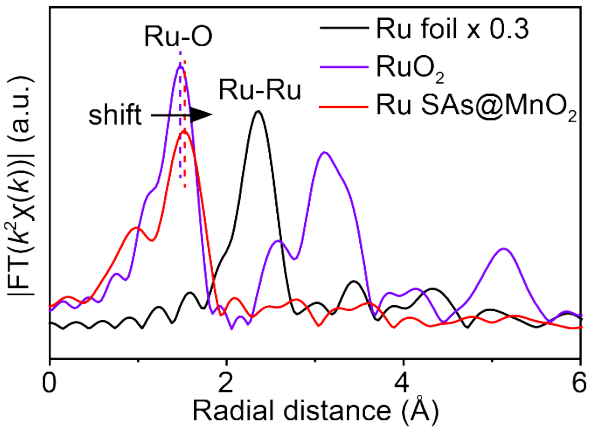

Fig. S5 The normalized Ru K-edge FT-EXAFS spectra of Ru foil, RuO_2, and Ru SAs@MnO_2.

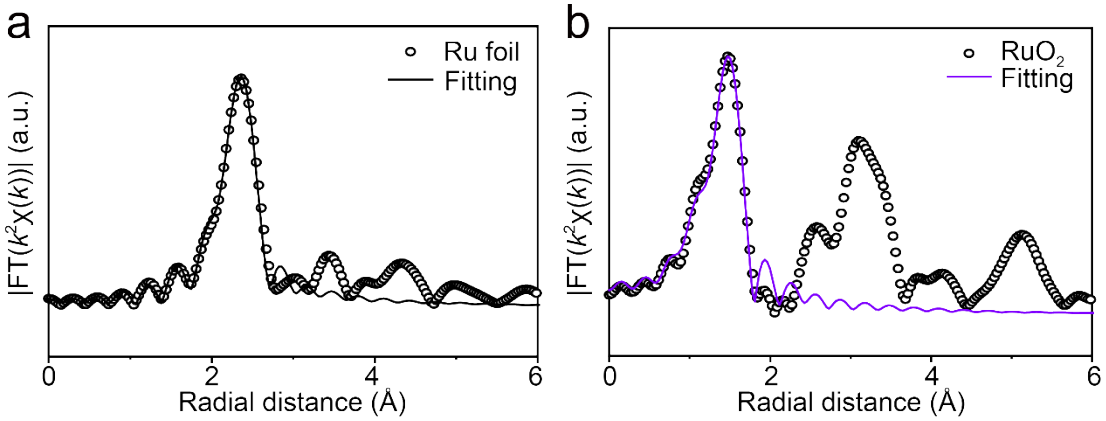

Fig. S6 The fitting of FT-EXAFS spectra of Ru foil and RuO_2 in R space.

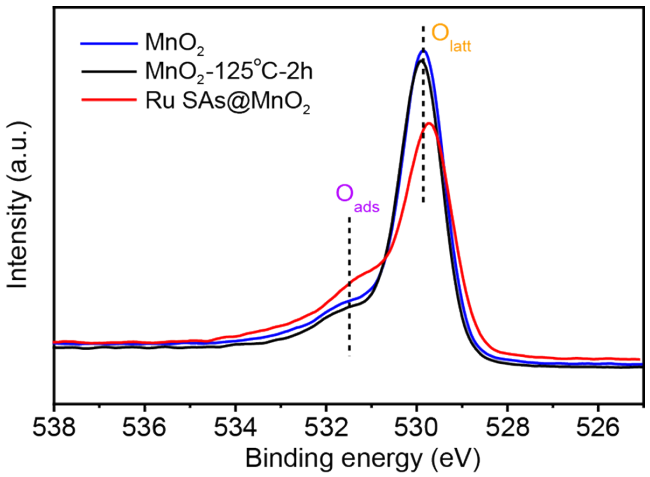

Fig. S7 The high-resolution XPS spectrum of O 1s in Ru SAs@MnO_2, MnO_2 and MnO_2 annealed under the same conditions without Ru source.

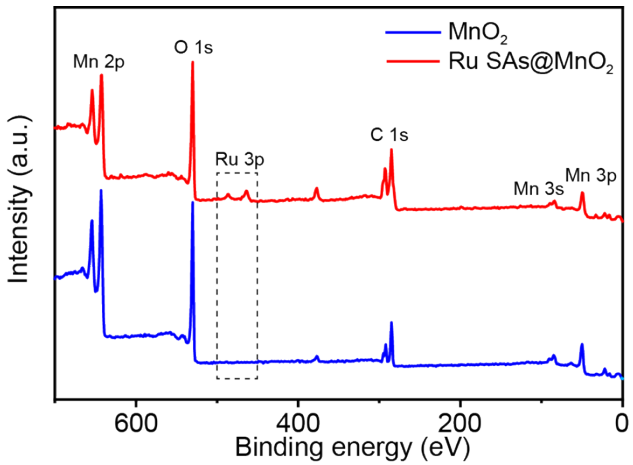

Fig. S8 XPS survey spectra of Ru SAs@MnO_2 and MnO_2 samples.

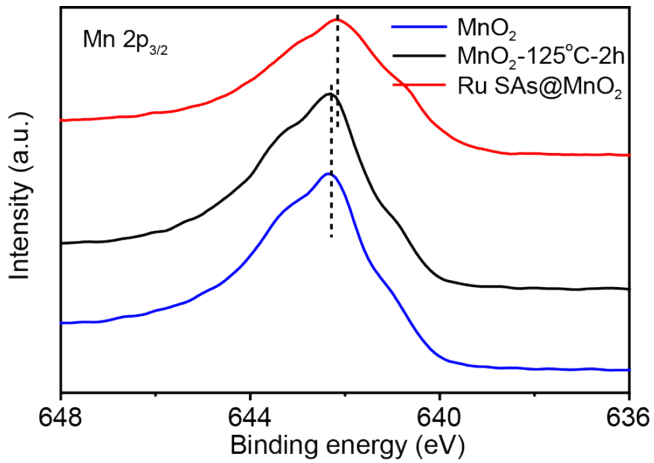

Fig. S9 The high-resolution Mn $2p_{3/2}$ XPS spectra of Ru SAs@MnO_2, MnO_2 and MnO_2 annealed under the same conditions without Ru source.

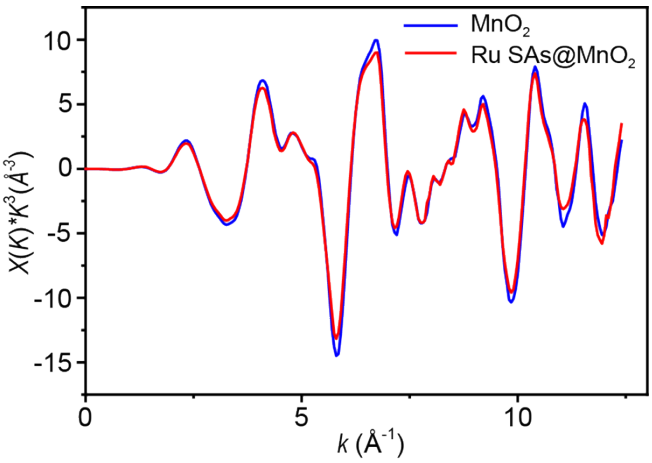

Fig. S10 FT-EXAFS curves at k space for Ru SAs@MnO_2 and MnO_2 samples.

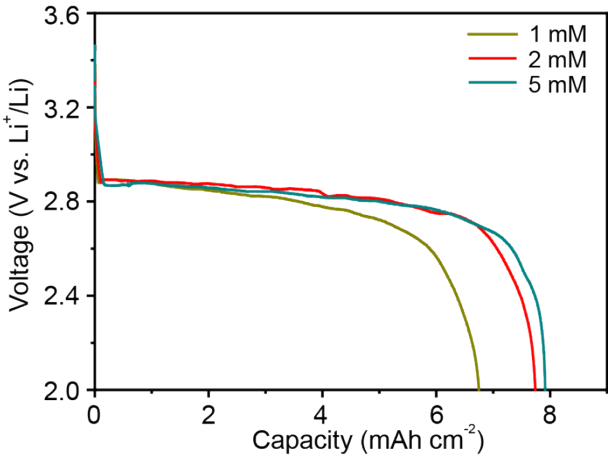

Fig. S11 The galvanostatic voltage profiles of the Ru SAs@MnO_2 prepared by 1 mM, 2 mM, and 5 mM $RuCl_3$ concentrations during deep discharge process a current density of 0.05 mA cm^{-2}.

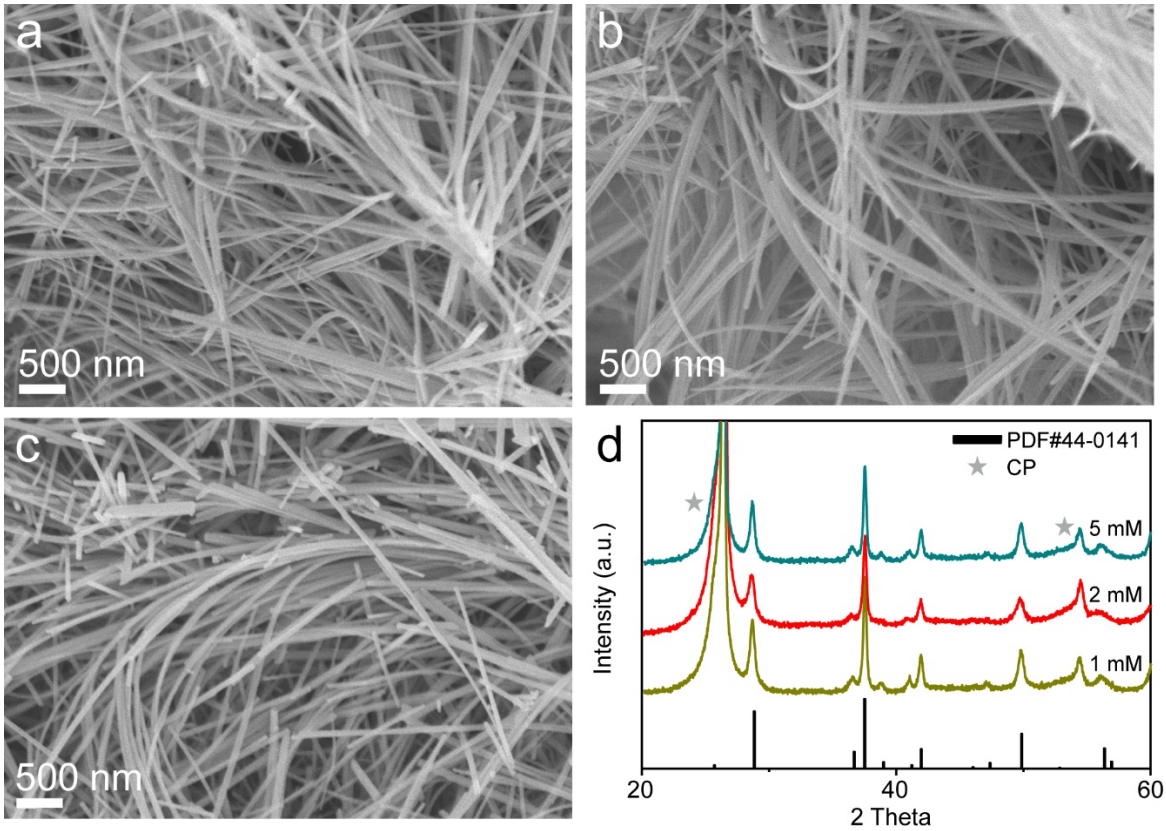

Fig. S12 SEM images of the Ru SAs@MnO_2 prepared by (a) 1 mM, (b) 2 mM, and (c) 5 mM $RuCl_3$ concentrations, respectively. (d) The corresponding XRD patterns of above samples.

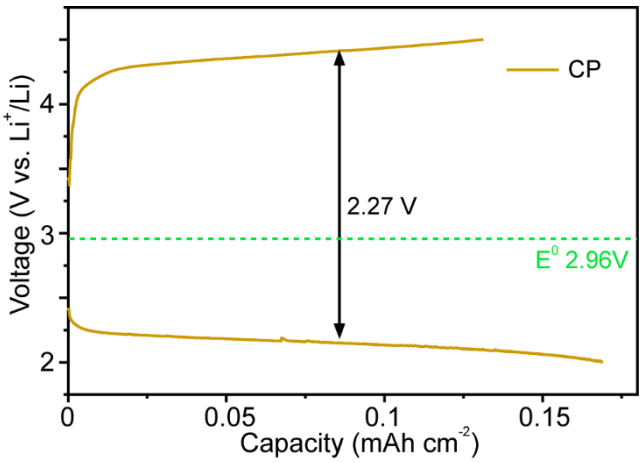

Fig. S13 The deep discharge/charge curves of CP collected at a current density of 0.1 mA cm^{-1}.

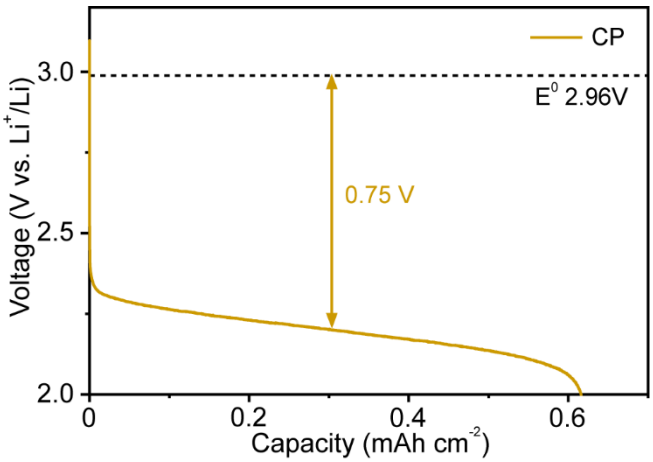

Fig. S14 The galvanostatic voltage profiles of the CP during deep discharge process a current density of 0.05 mA cm^{-2}.

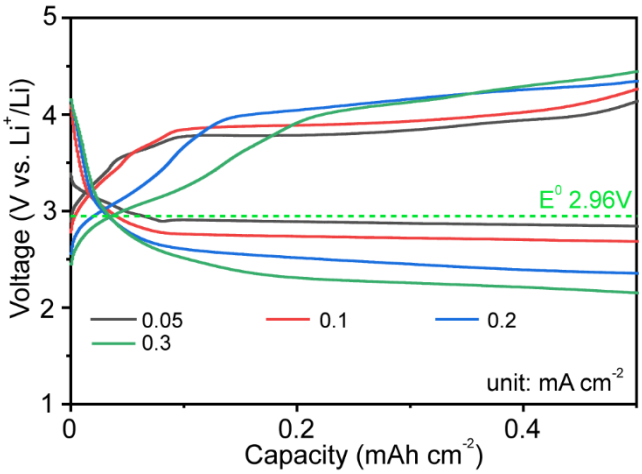

Fig. S15 The discharge/charge curves of MnO_2 collected at various current densities under a curtailing capacity of 0.5 mAh cm^{-2}.

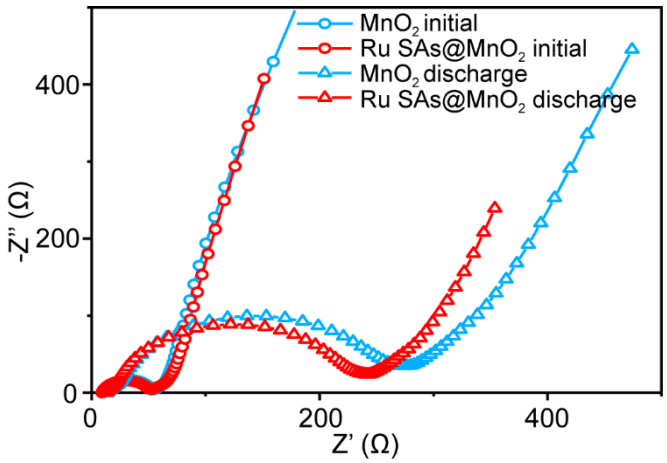

Fig. S16 The cycling performance of Ru SAs@MnO_2 and MnO_2 electrodes at a current density of 0.1 mA cm^{-2} under a cut-off capacity of 1 mAh cm^{-2}.

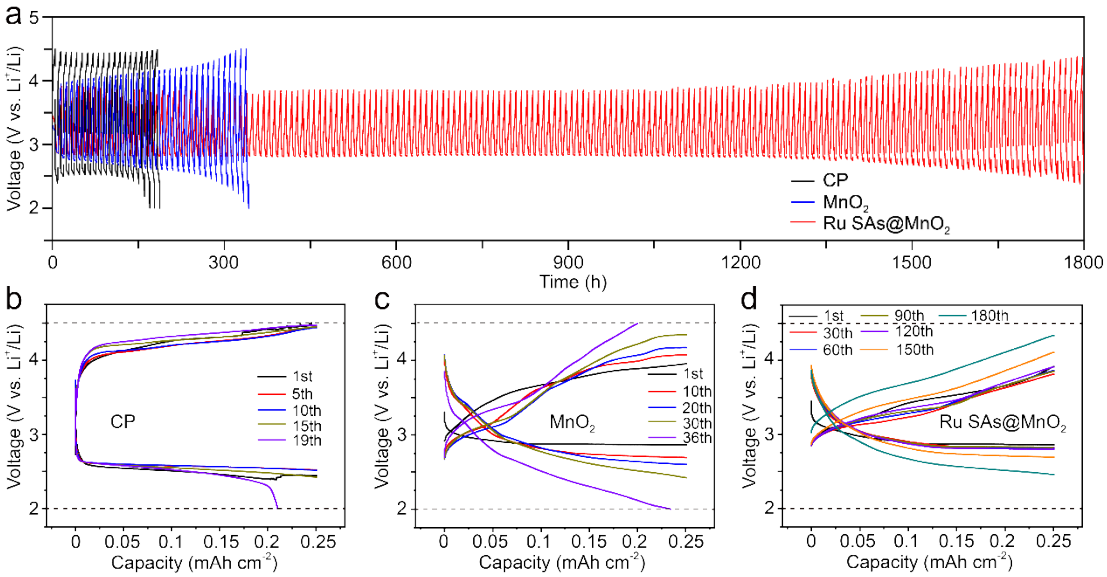

Fig. S17 (a) Voltage versus time curves of Ru SAs@MnO_2, MnO_2, and CP electrodes collected at the current of 0.05 mA cm^{-2} with the cut-off capacity of 0.25 mAh cm^{-2}. The discharge–charge curves of (b) CP, (c) MnO_2, and (d) Ru SAs@MnO_2 electrodes at various cycle numbers.

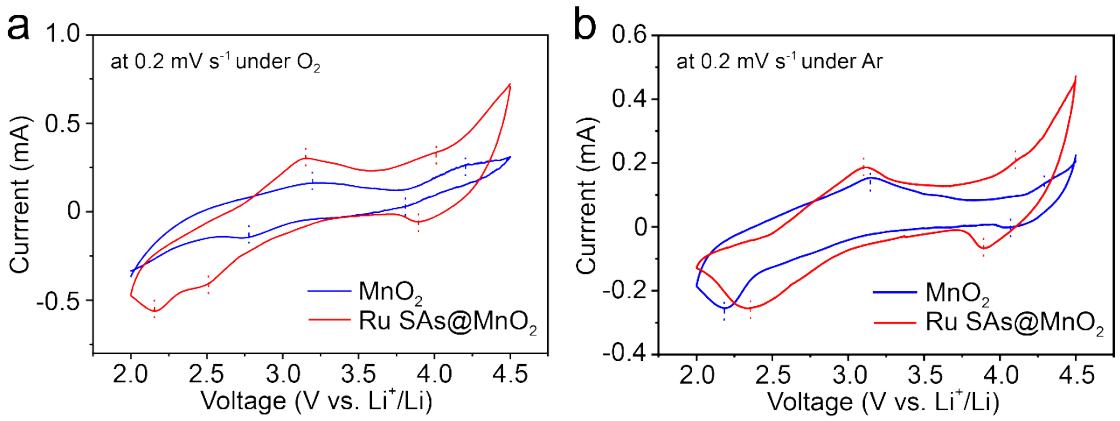

Fig. S18 CV curves of Ru SAs@MnO_2 and MnO_2 electrodes collected at the scan rate of 0.2 mV s^{-1} after 20 cycles.

As shown in Fig. S18a, although no additional redox peak appears, the CV curves of MnO_2 and Ru SAs@MnO_2 exhibit dramatic differences under O_2 atmosphere, especially in the cathodic region around 2.5 V, indicating huge differences in electrochemical behaviour, which are caused by the phase transition and dissolution of MnO_2. This electrochemical behaviour induced by the phase transition will eventually lead to battery failure. In addition, the Ru SAs@MnO_2 holds much larger cathodic/anodic peak currents compared with MnO_2, which can be attributed to the superior ORR/OER catalytic effect of the asymmetrical Mn-Ru dual-sites in the Ru SAs@MnO_2 electrode. Furthermore, the CV curves of different samples under Ar atmosphere also provided to exclude the effect of oxygen catalytic reaction (Fig. S18b). Apparently, the redox peak position of MnO_2 changes dramatically after 20 cycles, indicating an irreversible phase change. These results demonstrate the excellent stabilization and catalytic effect of asymmetrical Mn-Ru dual-sites on MnO_2 for ORR/OER reaction.

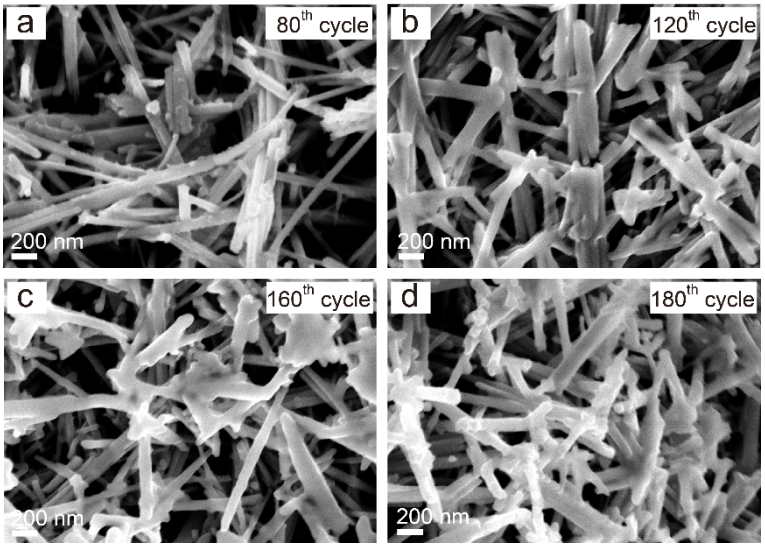

Fig. S19 The SEM images of Ru SAs@MnO_2 collected after (a) 80, (b) 120, (c) 160, and (d) 180 cycles, respectively.

Apparently, the Ru SAs@MnO_2 maintains mainly the nanowire morphology even after 180 cycles, despite the presence of a small number of nanoparticles.

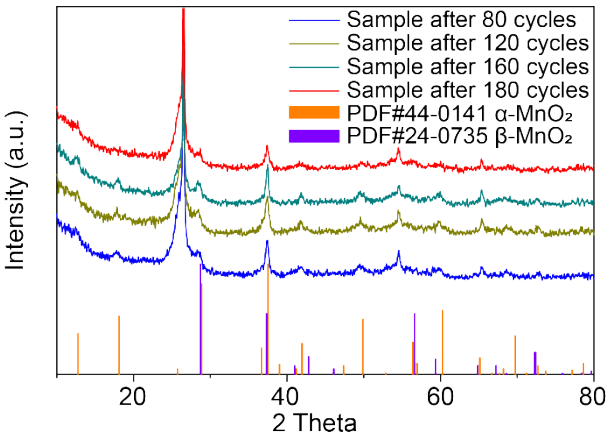

Fig. S20 The XRD patterns of Ru SAs@MnO_2 collected after 80, 120, 160, 180 cycles.

The XRD results show that the crystal structure of the Ru SAs@MnO_2 nanowires can be well maintained as α-MnO_2 during the cycling process. Notably, the peak intensity of Ru SAs@MnO_2 weakened after 180 cycles, indicating that the decay of the cyclic stability may be caused by structural degradation of MnO_2.

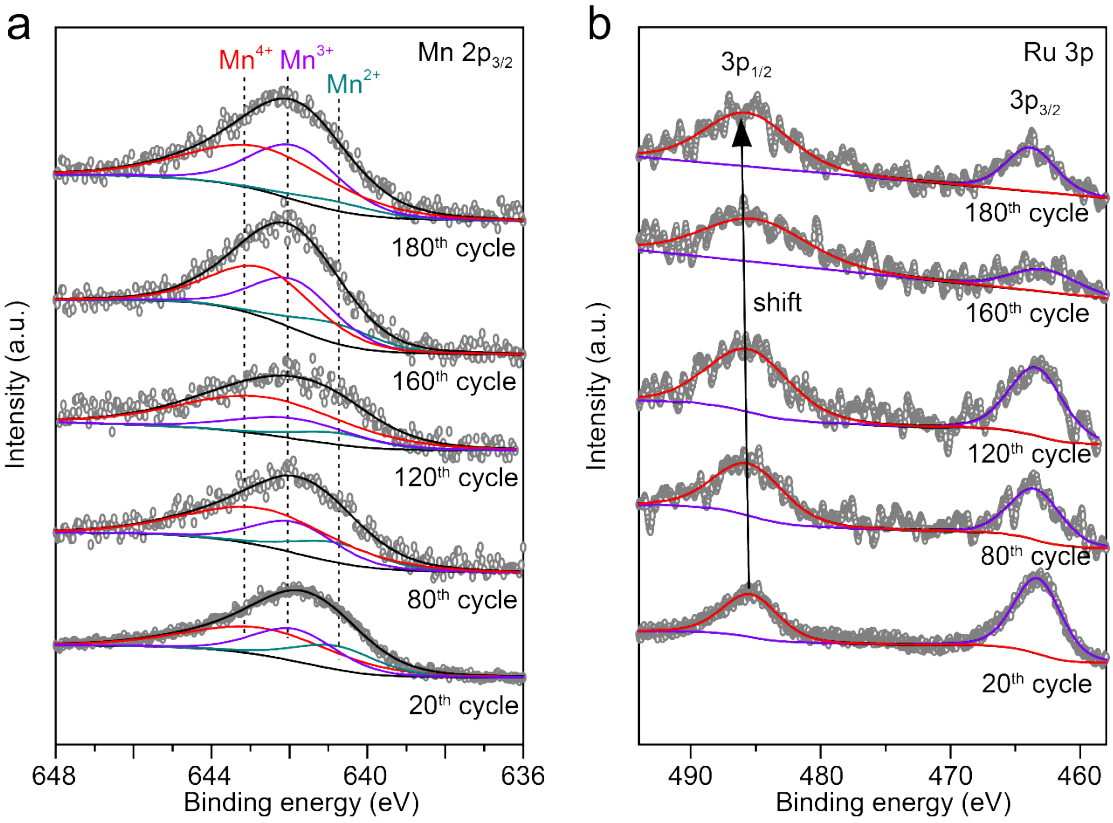

Fig. S21 XPS core-level (a) Mn $2p_{3/2}$ and (b) Ru 3p spectra of Ru SAs@MnO_2 collected after 20, 80, 120, 160, 180 cycles.

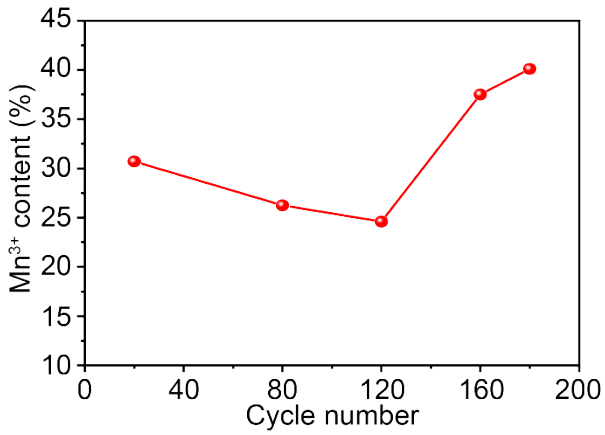

Fig. S22 The Mn^{3+} content of Ru SAs@MnO_2 collected after 20, 80, 120, 160, 180 cycles.

As shown in Fig. S18a, a small amount of Mn^{2+} corresponding to 640.8 eV appears during the cycling in addition to Mn^{4+} and Mn^{3+}. Notably, the state of Mn^{4+} is the main feature of Ru SAs@MnO_2 during the cycling process, indicating that the main component of Ru SAs@MnO_2

is still MnO_2. Considering that the Jahn-Teller effect of the Mn^{3+} causes the structural degradation of the manganese oxides, we analyze in detail the evolution of the Mn^{3+} content on the surface of Ru SAs@MnO_2 after various number of cycling tests (Fig. S19). Apparently, there is no significant change in Mn^{3+} content after 120 cycles, however, the surface Mn^{3+} content of Ru SAs@MnO_2 increased significantly after 160 cycles, which corresponds to a significant performance decay at around 160 cycles, indicating that the decay of cycling stability of Ru SAs@MnO_2 may be related to the increase in Mn^{3+} content. In addition, as shown in Fig. S18b, the Ru 3p signal was always existent during cycling, proving the stability of the Ru sites. It is noteworthy that Ru 3p shifts toward higher binding energy as the cycle proceeds, indicating a gradual rise in the oxidation state of Ru and a decrease in the average electron density around Ru sites, which may be due to the change in the electron density of the Mn sites.

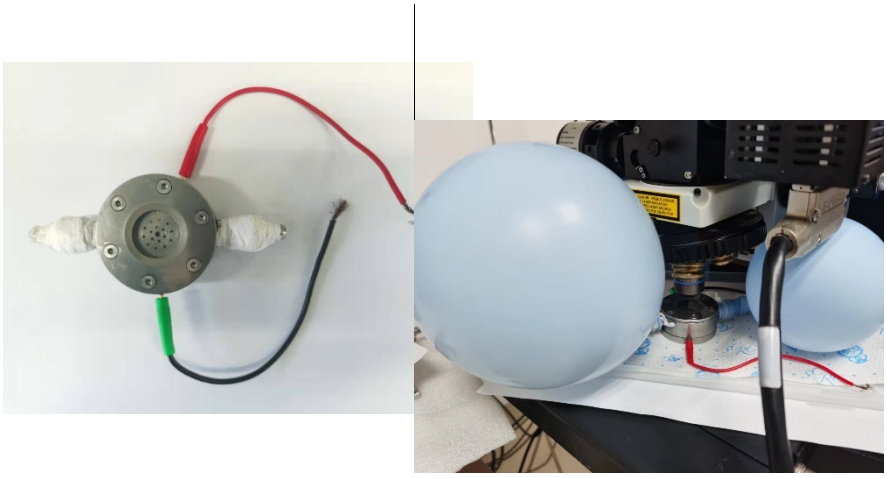

Fig. S23 The photographs of the *operando* Raman devices for Li-O_2 cell.

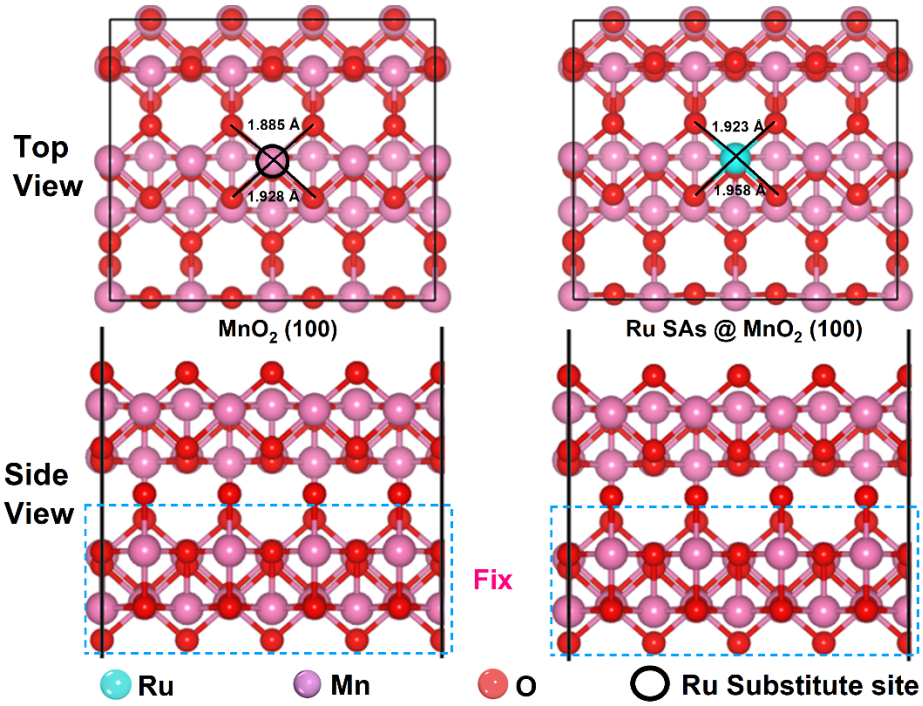

Fig. S24 The configurations of Ru SAs@MnO_2(100) and MnO_2(100) surface with bond length information.

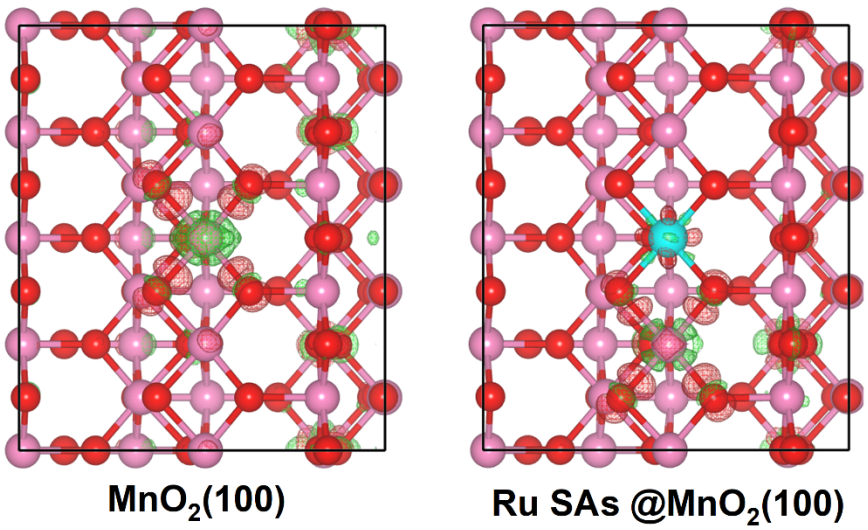

Fig. S25 3D charge density differences maps, $\Delta\rho = \rho_{(slab)} - \rho_{(Mn)} - \rho_{(slab-Mn)}$, on MnO_2 (100) and Ru SAs@MnO_2 (100), respectively. blue stands for negative, red stands for positive.

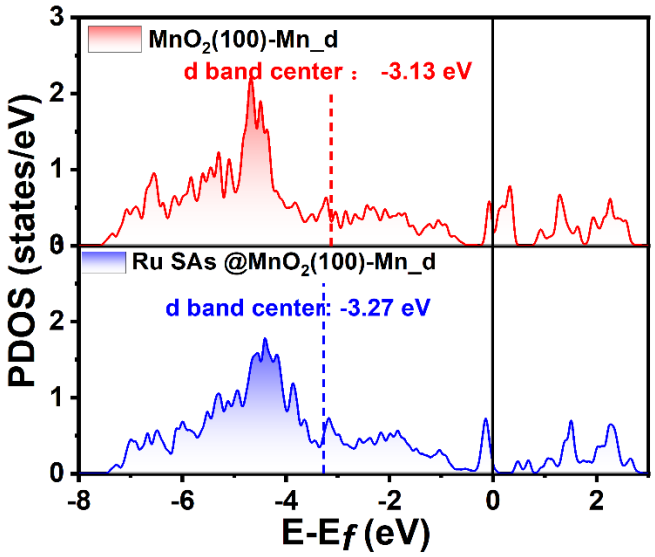

Fig. S26 The PDOS and corresponding d-band centers of Mn 3d on the surface of MnO_2 (100) and Ru SAs@MnO_2 (100).

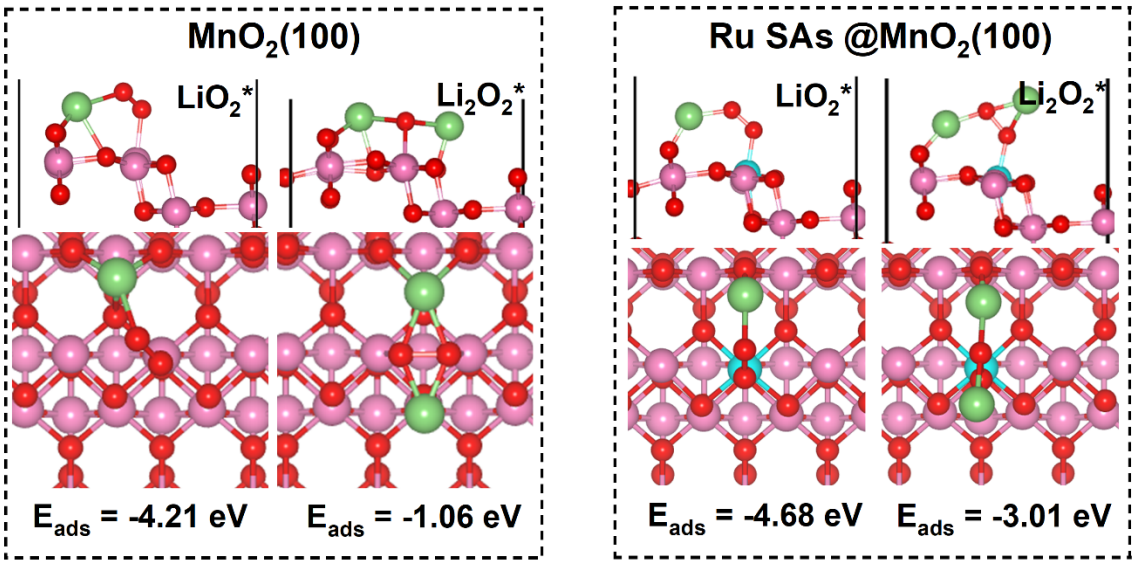

Fig. S27 The adsorption energy of oxygenated species (LiO_2* and Li_2O_2*) on MnO_2 (100) and Ru SAs@MnO_2 (100) and the corresponding adsorption configurations.

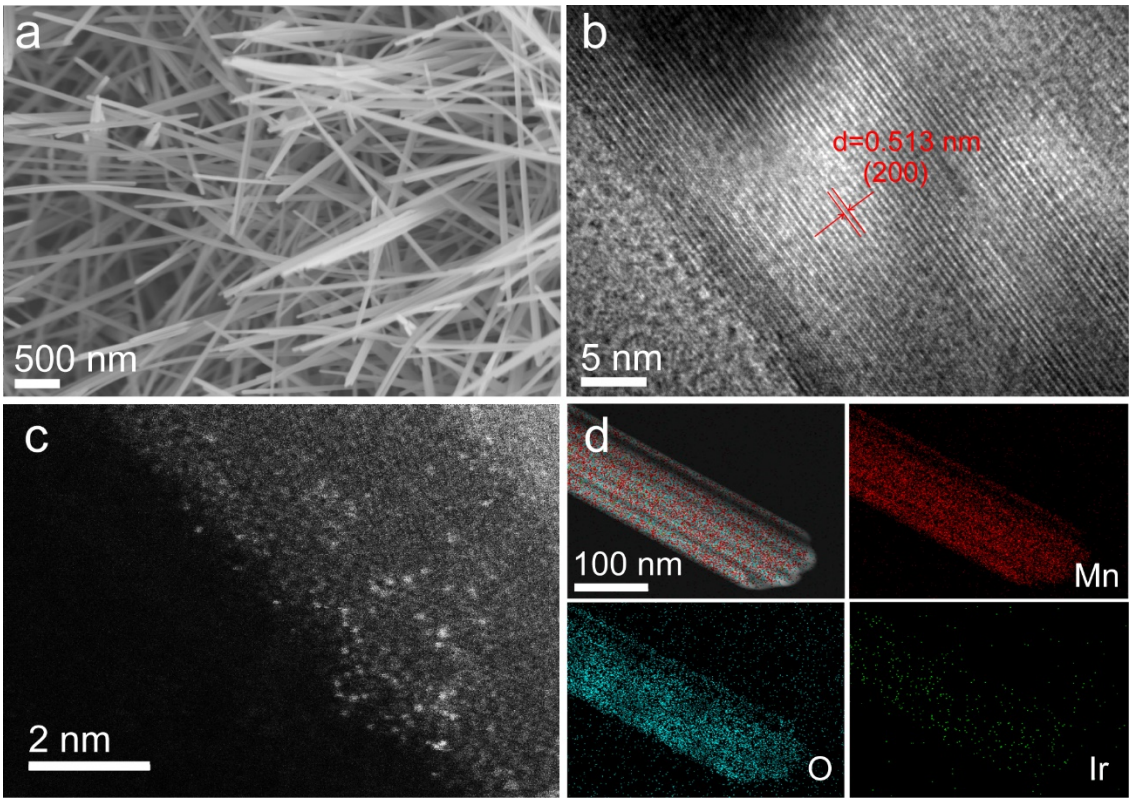

Fig. S28 (a) SEM and (b) HR-TEM images of Ir SAs@MnO_2 nanowires. (c) Aberration-corrected HAADF-STEM image of Ir SAs@MnO_2. (d) HAADF-STEM image of Ir SAs@MnO_2 and the corresponding EDX elemental mapping images.

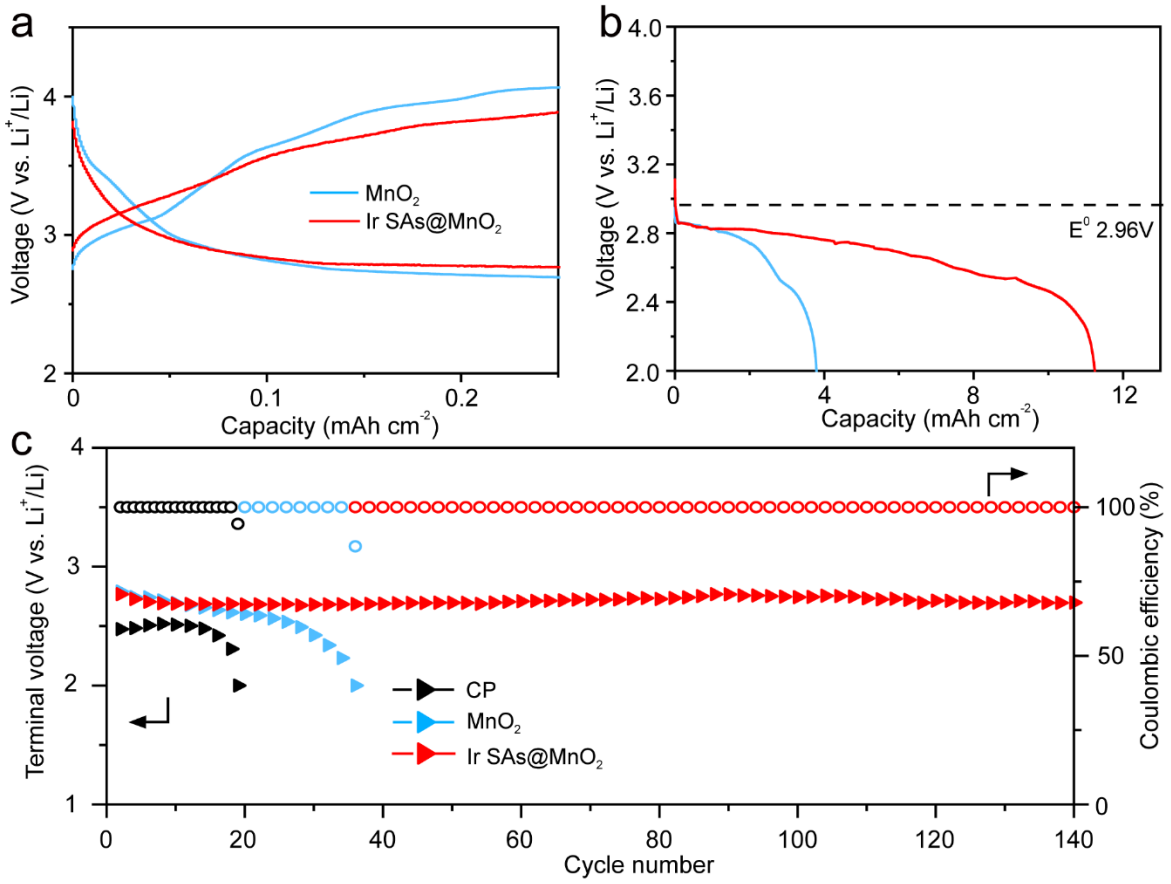

Fig. S29 (a) The discharge–charge curves of Ru SAs@MnO_2 and MnO_2 electrodes at a curtailed capacity of 0.25 mAh cm^{-1} at a current density of 0.05 mA cm^{-2}. (b) The galvanostatic profiles for the Ir SAs@MnO_2 and MnO_2 electrodes under full discharging at 0.05 mA cm^{-2}. (c) Cycling performances of Ir SAs@MnO_2, MnO_2, and CP electrodes collected at the current of 0.05 mA cm^{-2} with the cut-off capacity of 0.25 mAh cm^{-2}.

Table S1. The ICP-OES results of the Ru SAs@MnO_2 sample.

Sample	Ru amount (wt.%)
Ru SAs@MnO_2	1.9

Table S2. EXAFS fitting parameters at the Ru K-edge for various samples（S_0^2=0.700）

Sample	Shell	N^a	R(Å)^b	σ^2(Å^2)^c	ΔE_0(eV)^d	R factor
Ru foil-Refer	Ru-Ru	12	2.67±0.00	0.0030±0.0003	-6.1±0.1	0.0082
RuO_2-Refer	Ru-O	5.6±1.0	1.97±0.02	0.0016±0.0018	-3.5±2.4	0.0045
Ru SAs@MnO_2	Ru-O	5.0±2.3	2.02±0.04	0.0022±0.0060	2.8±5.4	0.0051

^aN: coordination numbers; ^bR: bond distance; $^c\sigma^2$: Debye-Waller factors; $^d\Delta E_0$: the inner potential correction. R factor: goodness of fit. S_0^2 was set to 0.700, according to the experimental EXAFS fit of Ru foil reference by fixing coordination numbers as the known crystallographic value.

Table S3. The Mn $2p_{3/2}$ XPS peak fitting parameters for Mn $2p_{3/2}$ spectra.

Samples	**Binding energy ($2p_{3/2}$)**	**Assignment**	**FWHM**	**Area**	**Area ratio of Mn^{3+}/Mn^{4+}**
MnO_2	641.90	Mn^{3+}	1.70	18360.64	17.0%
	642.70	Mn^{4+}	2.79	107728.30	
Ru SAs@MnO_2	641.85	Mn^{3+}	1.90	35315.90	64.2%
	642.65	Mn^{4+}	2.80	54984.11	

Table S4. EXAFS fitting parameters at the Mn K-edge for various samples（S_0^2=0.850）

Sample	Shell	N^a	R(Å)^b	σ^2(Å^2)^c	ΔE_0(eV)^d	R factor
MnO-Refer	Mn-O	6	2.20±0.02	0.0085±0.0015	-2.4±2.3	0.0057
	Mn-Mn	12	3.13±0.01	0.0087±0.0005	-5.5±1.1	
MnO_2-Refer	Mn-O	6.0	1.90±0.01	0.0065±0.0020	-5.7±1.5	0.0019
	Mn-Mn	4.0	2.88±0.01	0.0043±0.0028	-9.7±2.1	
MnO_2	Mn-O	5.7±1.1	1.90±0.01	0.0051±0.0024	-5.2±3.1	0.0018
	Mn-Mn	4.0±1.5	2.89±0.02	0.0033±0.0036	-8.5±3.2	
Ru SAs@MnO_2	Mn-O	5.2±1.8	1.93±0.01	0.0048±0.0031	-1.1±4.2	0.0066
	Mn-Mn	3.9±1.2	2.92±0.03	0.0043±0.0053	-6.8±4.4	

$^a N$: coordination numbers; $^b R$: bond distance; $^c \sigma^2$: Debye-Waller factors; ^{d} ΔE_0: the inner potential correction. R factor: goodness of fit. S_0^2 was set to 0.850, according to the experimental EXAFS fit of MnO reference by fixing coordination numbers as the known crystallographic value.

Table S5. Comparison of the overpotentials and cycling stability between the Ru SAs@MnO_2 catalyst and other Mn-based and noble-metal-based catalysts in previous reports.

	Sample	Overpotentials	Cycling stability	Ref.
Ru SAs@MnO_2		**0.69 V at 0.05 mA cm^{-2}**	**0.05 mA cm^{-2}, 0.25 mAh cm^{-2} for 180 cycles (1800 h)**	**This work**
Mn-based	selenate-anchored α-MnO_2	～1.4 V at 200 mA g^{-1}	4.2 V, 1000 mAh g^{-1} for 70 cycles	*Angew. Chem. Int. Ed.* 2018, **57**, 15984-15989
	β-MnO_2 (100 facets)	～1.19 V at 0.05 mA cm^{-2}	/	*J. Am. Chem. Soc.* 2019, **141**, 12832-12838.
	Pd/δ-MnO_2	0.65 V at 100 mA g^{-1}	200 mA g^{-1}, 1000 mAh g^{-1} for 133 cycles (1330h)	*Energy Storage Mater.* 2018, **12**, 8-16.
	α-MnO_2/RuO_2 @GN	0.49 V at 100 mA g^{-1}	100 mA g^{-1}, 1000 mAh g^{-1} for 45 cycles (900h)	*ACS Catal.* 2018, **8**, 7983-7990
Noble-metal-based	PtAu	> 0.36 V at 100 mA g^{-1}	500 mA g^{-1}, 1000 mAh g^{-1} for 220 cycles (> 850h)	*Angew. Chem. Int. Ed.* 2022, **134**, e202201416
	PtIr	0.44 V at 100 mA g^{-1}	500 mA g^{-1}, 1000 mAh g^{-1} for 180 cycles (> 700h)	*Angew. Chem. Int. Ed.* 2021, **60**, 26592-26598
	Pd	0.2 V at 200 mA g^{-1}	200 mA g^{-1}, 1000 mAh g^{-1} for 70 cycles (700h)	*ACS Catal.* 2018, **8**, 9006-9015
	PdNi	1.05 V at 300 mA g^{-1}	300 mA g^{-1}, 1000 mAh g^{-1} for 67 cycles (450h)	*J. Mater. Chem. A* 2018, **6**, 10856-10867

Pd/CNTs	～0.4 V at 0.05 mA cm^{-2}	0.05 mA cm^{-2}, 0.5 mAh cm^{-2} for 50 cycles (1000h)	*ACS Energy Lett.* 2019, **4**, 2782-2786
Pt_3Co	0.2 V at 100 mA g^{-1}	100 mA g^{-1}, 5000 mAh g^{-1} for 300 cycles (3000h)	*Energy Storage Mater.* 2020, **24**, 707-713
Ru SAs-NC	0.55 V at 0.02 mA cm^{-2}	0.02 mA cm^{-2}, 1000 mAh g^{-1} for 60 cycles	*J. Am. Chem. Soc.* 2020, **142**, 16776-16786

Table S6. d-band centre values of Mn atoms on MnO_2 (100) and Ru SAs@MnO_2 (100) surfaces.

Atoms	MnO_2(100)	Ru SAs @MnO_2 (100)
Mn_1	-3.13 eV	-3.27 eV
Mn_2	-3.13 eV	-3.27 eV

Mn_1 and Mn_2 are the Mn atoms around the substituted Ru atom on MnO_2 (100) surface (Fig. S26).

Table S7. Bader Charge on the MnO_2 (100) and Ru SAs @MnO_2(100) surfaces, respectively.

Bader/*e*	Mn^{3+}/*e*	Ru/*e*
MnO_2(100)	-1.73	--
Ru SAs@MnO_2(100)	-1.71	-1.82

Table S8. ICOHP value of Mn-O and Ru-O bonds on the surfaces of MnO_2 (100) and Ru SAs@MnO_2(100).

ICOHP/eF	MnO_2(100)	Ru SAs @MnO_2 (100)
Mn-O	-1.03	-1.10
Ru-O	--	-2.21

eF: Strength of the bond relative to the Fermi energy level;

References

[1] Y. Hu, G. Luo, L. Wang, X. Liu, Y. Qu, Y. Zhou, F. Zhou, Z. Li, Y. Li, T. Yao, *Adv. Energy Mater.* 2021, **11**, 2002816.

[2] G. Meng, H. Tian, L. Peng, Z. Ma, Y. Chen, C. Chen, Z. Chang, X. Cui, J. Shi, *Nano Energy* 2021, **80**, 105531.